symmetry

IMPACT FACTOR 2.940

CITESCORE 4.3

Article

Nuclear Structure Investigations of Even–Even Hf Isotopes

Polytimos Vasileiou, Theo J. Mertzimekis, Eirene Mavrommatis and Aikaterini Zyriliou

Special Issue
Selected Papers from Shapes and Symmetries in Nuclei: From Experiment to Theory (SSNET'21 Conference)

Edited by
Prof. Dr. Costel Petrache and Prof. Dr. Jerzy Dudek

MDPI

https://doi.org/10.3390/sym15010196

symmetry

Article

Nuclear Structure Investigations of Even–Even Hf Isotopes

Polytimos Vasileiou *, **Theo J. Mertzimekis**, **Eirene Mavrommatis** and **Aikaterini Zyriliou**

Department of Physics, Zografou Campus, National & Kapodistrian University of Athens, GR-15784 Zografou, Greece
* Correspondence: polvasil@phys.uoa.gr

Abstract: The mass region of rare-earth nuclei in the nuclear chart is riddled with well-deformed nuclei, exhibiting rotational properties and many interesting nuclear structure-related phenomena. The scarcity of experimental data as the neutron number increases and the exotic phenomena such as shape coexistence, which are strongly connected with the underlying symmetries of the Hamiltonian and are predicted to take place in this region, make this mass region a fertile ground for experimental and theoretical studies of nuclear structure. In this work, we investigate the structure of the even–even $^{162\text{–}184}$Hf (hafnium) isotopes through a calculation of various observables such as $B(E2; 0_1^+ \to 2_1^+)$ reduced transition matrix elements and quadrupole moments. Six different nuclear models are employed in the calculations of the observables for these nuclei, the shapes of which deviate from spherical symmetry, and as such, are characterized by Hamiltonians, which break the rotational invariance of the exact nuclear many-body Hamiltonian. The results of the present study are expected to establish some concrete guidelines for current and future experimental endeavors. Along these lines, the results for the $^{162\text{–}180}$Hf isotopes are compared with existing experimental data where available, showing an overall good agreement.

Keywords: even–even Hf isotopes; theoretical models; quadrupole moments; $B(E2)$ transition rates

Citation: Vasileiou, P.; Mertzimekis, T.J.; Mavrommatis, E.; Zyriliou, A. Nuclear Structure Investigations of Even–Even Hf Isotopes. *Symmetry* **2023**, *15*, 196. https://doi.org/10.3390/sym15010196

Academic Editors: Costel Petrache and Jerzy Dudek

Received: 6 December 2022
Revised: 29 December 2022
Accepted: 4 January 2023
Published: 9 January 2023

1. Introduction

Over the past decade, the study of nuclear structure has regained a dominant role in nuclear physics, mainly due to the discovery of new physics, occurring far outside the traditionally studied valley of stability. The discoveries, which resulted from groundbreaking innovations in radioactive beam production, have posed multiple questions regarding the fundamental interactions among the nucleons, i.e., the protons and neutrons under extreme conditions. Filling the large gaps in the knowledge has a critical impact on understanding the evolution of the Universe driven by nuclear reaction networks in bodies in the Universe (such as the *s*- or *r*-processes) [1] and putting together the puzzle of the particle constituents that shape nuclear matter.

The massive shift in the nuclear physics scientific community toward using Radioactive Ion Beams (RIBs) to explore new phenomena and test existing symmetries, investing significant effort in establishing the outer limits of the nuclear chart and the properties of the exotic species inhabiting those mass regimes (see, for instance, Ref. [2]), has left large gaps in the knowledge of the mass region lying between the valley of stability and the nuclear driplines. In particular, the isotopes located in the $A \approx 140\text{–}180$ mass regime to the east of the valley of stability are of special interest, as they feature low-lying isomeric states [3,4], shape coexistence [5,6], and sizeable deformations, which can be attributed to the shape of nuclear potential, new prevailing symmetries, and, often, the appearance of octupole collectivity [6–10].

Deformed nuclei can be schematically categorized as *prolate*, *oblate*, and *triaxial*—a direct consequence of the nuclear dynamic symmetries of the deformed Hamiltonian—based on the three principal axes of rotation in the ellipsoid. These symmetries regarding the nuclear shapes are clearly reflected on the $\beta\gamma$ plane formed by the set of intrinsic shape variables (β, γ) entering the Bohr Hamiltonian. This plane is subdivided into six equivalent parts based on the symmetries. All of the shapes are uniquely contained in the $\gamma = (0^\circ, 60^\circ)$ sector, which can be taken as the representative one. *Prolate* nuclei lie on the $\gamma = 0^\circ$ axis, *oblate* nuclei lie on the $\gamma = 60^\circ$ axis, whereas the nuclei located in between the $\gamma = 0^\circ$ and $\gamma = 60^\circ$ are *triaxial*. These shapes are repeated in each of the remaining subsectors of the $\beta\gamma$ plane, alternating between the principal symmetry axes [11,12].

Many nuclei in the rare-earth region of the nuclear chart are known to be well deformed, often exhibiting quadrupole deformation parameter values $\beta_2 > 0.2$ for the ground or low-lying states [4]. It is common for the nuclei in this mass region to show a collective character with rotational properties, where the energy spectra can be approximated by the relation $E \propto I(I+1)$ (I: total spin) [11]. As nuclear rotations can alter the microscopic structure of nuclei, the preferred shapes of nuclei typically change as the spin increases. This is very common for the "soft" nuclei. In any case, a mixed character (both rotational and vibrational) can be present in many nuclei.

Over the past few decades, numerous theoretical approaches have attempted to study such phenomena including semi-empirical methods, mean-field and beyond mean-field models such as the particle-rotor model [13], the cranked shell model [14–16], the projected shell model [17], the cranking covariant density functional theory [18], and more. All such theoretical directions, one way or another, provide the means to study the nuclear structure evolution imposed by the underlying symmetries.

From an experimental standpoint, several observables can provide stringent tests of the existing theoretical models in an effort to gain insight into the nuclear structure. $B(E2)$ reduced electric transition probabilities are some of the most prominent among them, having been proven particularly useful in the task of understanding the collective behavior of deformed nuclei. Their direct relation to the nuclear state lifetimes allows for their determination through a variety of experiments, providing valuable information on the interplay between collective and single-particle degrees of freedom.

In the 1960s, at Oak Ridge National Laboratory, P. H. Stelson and L. Grodzins recognized the importance of the compilation and evaluation of $B(E2)$ transition probabilities for even–even nuclei and moved on to produce the first compilation of $B(E2) \uparrow$ values for the 2_1^+ nuclear states [19]. The next two compilations and evaluations were carried out in 1987 [20] and 2001 [21] by Raman et al. in the framework of the Oak Ridge Nuclear Data Project prior to the successful launch of the Brookhaven $B(E2) \uparrow$ project [22] in 2005. The NNDC database currently contains a compilation of updated $B(E2; 0_1^+ \rightarrow 2_1^+)$ experimental results and evaluated values. A detailed upgrade of the database with the experimental reduced matrix elements, $B(E2) \uparrow$s, and mean lifetimes, $\tau(2_1^+)$, was carried out by Pritychenko et al. [23,24]. Table I in [23] contains experimental values for nuclei with $Z = 2$–104, whereas their adopted values, together with deformation β_2, are shown in Table III of the same reference.

In this work, the rotational properties of the well-deformed even–even $^{162\text{–}184}$Hf nuclei are investigated through calculations of their electric quadrupole moments and reduced electric quadrupole probabilities using various theoretical models. Neutron-rich Hf isotopes are located in the upper half of the $Z = 50$–82 proton shell and the $N = 82$–126 neutron shell, and in this region, multi-particle excitations are expected to be increasingly preferred. Regarding the theoretical models employed in this work, except for the phenomenological model and finite-range droplet model described in Sections 3.1 and 3.2, respectively, they are based on a mean-field description (non-relativistic or relativistic) and include a pairing. Mean-field Hamiltonians break the symmetries that the many-body Hamiltonians have. The symmetries that are, in general, broken include the translational, rotational, reflection, and isospin symmetries [25,26]. As for the methods used to incorporate the pairing (Bardeen–Cooper–Schrieffer or Bogoliubov), they do not conserve the particle number. Several techniques have been proposed to restore the broken symmetries to some extent (see, for example, Refs. [25,27]).

The results for the Hf isotopes are extended to $A = 182, 184$ for which there currently exist no experimental data for the 2_1^+ states other than the energies $E(2_1^+)$ (it should be noted that even the spin and parity of the 2_1^+ state are questionable in the case of ^{184}Hf) [23]. The results for the various calculated physical quantities are compared with previous works [28–30], as well as with the available experimental data [4,21,23,31].

In recent years, many theoretical studies have been conducted that are centered around the Hf isotopic chain and employ several different models (see, for example, Refs. [32,33]). This work aims to provide a complete set of predictions for the examined observables, with an emphasis on experimentally measurable quantities (such as lifetimes and $B(E2)$s), using a variety of theoretical models. These results are expected to guide future experimental and theoretical studies in the unstable neutron-rich Hf isotopes [34,35], as was the case for a similar study of Yb isotopes [36,37].

2. Physical Quantities and Global Best Fit

For nuclei featuring rotational spectra, the $B(E2)$ can be related directly to the intrinsic electric quadrupole moment, Q_0, and, in turn, be associated with the β_2 deformation parameters [11]. Furthermore, the $B(E2)$ is connected to the root mean square (rms) of the deformation β_2 in non-rotational regions. In the following paragraphs, we give some brief definitions of the various observables studied in this work, among which are the intrinsic quadrupole moments Q_0, the electric quadrupole moments Q, and the β_2 deformation parameters.

2.1. The Intrinsic Quadrupole Moment Q_0

The intrinsic quadrupole moment Q_0 is defined in the intrinsic frame of reference of the nucleus. Deviations from the spherical shape are associated with the intrinsic quadrupole moment Q_0, which is, in turn, related to the reduced electric quadrupole transition probability $B(E2)$ through the relation [11]

$$Q_0 = \left[\frac{16\pi}{5} \frac{B(E2)\uparrow}{e^2} \right]^{1/2} \tag{1}$$

where the upward-pointing arrow represents the excitation.

2.2. The Electric Quadrupole Moment Q

The electric quadrupole moment Q describes the apparent shape of the nuclear charge distributed over the ellipsoid volume. As a convention, negative values of Q in the laboratory frame are associated with prolate nuclear shapes, whereas positive values of Q are associated with oblate nuclei. A zero value for the electric quadrupole moment Q indicates spherically symmetric nuclear shapes [12]. In the framework of the nuclear shell model, spherical nuclear charge distributions are expected for closed shells; thus, the measurement of the electric quadrupole moment can serve as a test of the shell model itself. Since the quadrupole moment depends on the size and charge of the nucleus, a better comparison is obtained after normalization for those factors, resulting in what is called the "reduced quadrupole moment". A plot of measured values [38] reveals that magic numbers of neutrons and protons are associated with near-zero values of the quadrupole moment.

A single-nucleon transition model fails to accurately describe the quadrupole moments of strongly deformed nuclei. Such cases are more adequately described in the framework of a collective nuclear model, involving the collective motion of many nucleons within a given nucleus. In this model [11], the spectroscopic and intrinsic quadrupole moments are interconnected via the relation

$$Q = \frac{3K^2 - I(2I-1)}{(I+1)(2I+3)} Q_0 \tag{2}$$

where I is the total spin of the nucleus and K is the total projection of I onto the z-axis in the body fixed frame (symmetry axis of the nucleus). For $K = 0$, $I = 2$ one obtains

$$Q(2_1^+) = -\frac{2}{7}Q_0 \tag{3}$$

If the intrinsic deformation is prolate ($Q_0 > 0$), the corresponding quadrupole moment in the laboratory frame turns negative, reflecting the result of time averaging a twirled cigar shape, which becomes an oblate apparent shape [12]. We note that the ratio $R_{QB} \equiv Q(2_1^+)/\sqrt{B(E2^+)\uparrow} = -0.906$ in this model [39].

2.3. The Deformation Parameter β_2

The $B(E2)\uparrow$ values are basic experimental quantities, which are model independent. Another useful quantity, which is model dependent, is the β_2 deformation parameter. Under the assumptions that the charge distribution is uniform from the center to a distance $R(\theta, \phi)$ and zero beyond and that the deformations are small, we find that β_2, $B(E2)$, and Q_0 are related by the formula

$$\beta_2 = \left(\frac{4\pi}{3ZR_0^2}\right)\left[\frac{B(E2)\uparrow}{e^2}\right]^{1/2} = \frac{\sqrt{5\pi}}{3ZR_0^2}Q_0 \tag{4}$$

where $R_0 = 1.2A^{1/3}$ [fm]. In the theoretical description of the excitation of collective states through direct reactions, a similar parameter is involved to account for the deformation of the average potential. The latter is analogous to β_2, which involves single-particle effects, indicative of the existence of quadrupole collective motion in a nucleus. Thus, the ratio β_2/β_{SP} is often considered, where β_{SP} refers to the single-particle model given in [23]:

$$\beta_{SP} = \frac{1.59}{Z} \tag{5}$$

Before concluding this introductory subsection, we give a final relation between the observables studied in this work, namely the relation between the lifetimes τ and the $B(E2)$ reduced electric quadrupole transition probabilities. This relation, given below, is used to calculate the lifetimes $\tau(2_1^+)$ based on the $B(E2)$ values:

$$\tau = \frac{\tau_\gamma}{1 + a_T} = 40.81 \times 10^{13} E_\gamma^{-5}\left[\frac{B(E2)\uparrow}{e^2b^2}\right]^{-1}(1 + a_T)^{-1} \ \text{[ps]} \tag{6}$$

where E_γ are the energies of the emitted photons in keV and a_T are the internal conversion coefficients [21,23].

2.4. Global Best Fit

Based on the global systematics of available data, knowing the energy of the first 2_1^+ state, $E(2_1^+)$ is sufficient for a prediction of the corresponding $B(E2)\uparrow$ [e^{2}b^2] and τ_γ [ps] values [21]. Within the framework of the hydrodynamic model with irrotational flow, Bohr and Mottelson [40,41] derived simple expressions for the τ_γ values, namely

$$\tau_\gamma \approx 0.6 \times 10^{14} E^{-4} Z^{-2} A^{1/3} \ \text{[ps]} \tag{7}$$

for the small harmonic vibrations of spherical nuclei, and

$$\tau_\gamma \approx 1.4 \times 10^{14} E^{-4} Z^{-2} A^{1/3} \ \text{[ps]} \tag{8}$$

for the rotational degrees of freedom of axially symmetric nuclei [21]. Grodzins [42] adopted this $E^{-4}Z^{-2}$ dependence in the above expressions to perform empirical fits on all even–even nuclei and further replaced $A^{1/3}$ with A.

The above expressions have been updated and revised to establish the functional relationship between (E, A) and (E, τ_γ) that best describes the experimental data in Ref. [20]. The adopted values for τ_γ, excluding those for closed-shell nuclei, lead to the expression [21]:

$$\tau_\gamma = (1.59 \pm 0.28) \times 10^{14} E^{-4} Z^{-2} A^{2/3} \ \ [\text{ps}] \tag{9}$$

Using Equations (4) and (6), the corresponding $B(E2)\uparrow$ and β_2 predictions are given by [21]

$$B(E2)\uparrow = (2.57 \pm 0.45) E^{-1} Z^2 A^{-2/3} \ \ [\text{e}^2\text{b}^2] \tag{10}$$

and

$$\beta_2 = (466 \pm 41) E^{-1/2} A^{-1} \tag{11}$$

We should mention that in Ref. [43], an analysis of the evaluated data for the $B(E2)\uparrow$s in Ref. [23] has been performed using the "elemental" fit of Habs et al. [44], who introduced a modification to the $B(E2)$ formula of Raman et al. for nuclei located in the $50 \leq Z \leq 82$ region of the nuclear chart. Their fit performs better than the Global Best Fit of Raman et al. in some cases, however, it can lead to predictions of negative $B(E2)\uparrow$ values, with large uncertainties for neutron-rich nuclei (e.g., ^{26}O, ^{214,216,218}Po) (for a detailed discussion on the fits of Habs et al., see Refs. [43,44]). These non-physical predictions pose limits for the Habs formalism outside the $50 \leq Z \leq 82$ mass region, whereas Raman's formalism, albeit less accurate, is more robust and can safely be adopted across the nuclear chart.

The resulting values for the lifetimes $\tau(2_1^+)$, reduced transition probabilities $B(E2)\uparrow$, (intrinsic) quadrupole moments (Q_0) Q, and β_2/β_{SP} ratios are calculated using Equations (1)–(6) and are compared with the experimental data of Pritychenko et al. [23], as well as with the theoretical predictions presented in Section 3.

3. Theoretical Models

In this section, we briefly discuss each of the models employed in this study and refer occasionally to their symmetries. For a complete and detailed description of the models, please refer to the original works (see the References section). These models have been used for the calculation of reduced electric quadrupole transition probabilities, $B(E2)$, electric quadrupole moments Q_0 and Q, and the β_2 deformation parameters in the framework of the nuclear collective model. The results presented later in this section are compared with the available experimental data. In the case of the phenomenological model (see Section 3.1 below), the energy levels for the ground-state band of the $^{162-184}$Hf isotopes have been additionally determined. The structure of the excited levels is discussed in Sections 3.1 and 4.

3.1. Phenomenological Model (PhM)

The phenomenological nuclear adiabatic model described by A. Bohr and B.R. Mottelson [11] has been central to explaining the properties of deformed nuclei. In their model, the low-excitation states in even–even deformed nuclei are connected with the collective rotations in axially symmetric nuclei. Despite its simplicity, this phenomenological explanation allows for a description of a large set of experimental data for even–even deformed nuclei while offering predictions of the many new properties of these deformed nuclei.

In Refs. [28,29,45], a phenomenological model (PhM), which takes into account the non-adiabaticity effects, is proposed by considering the Coriolis mixing of the low-lying states of positive parity in rotational bands and thus breaking the axial symmetry. The aforementioned model has been implemented in this work to determine the energies of the excited levels of the ground-state bands in the deformed $^{162-184}$Hf nuclei.

The starting point for this model is a nuclear Hamiltonian of the form [28]

$$H = H_{rot} + H_{K,K'} \tag{12}$$

where H_{rot} is the rotational part of the Hamiltonian and

$$H_{K,K'} = \omega_K \delta_{K,K'} - \omega_{rot}(I)(j_x)_{K,K'}\chi(I,K)\delta_{K,K'+1} \tag{13}$$

with $(j_x)_{K,K'} = \langle K|j_x|K'\rangle$ being the matrix element of the Coriolis coupling of the rotational band members, $\omega_{rot}(I)$ the rotational frequency of the core, ω_K the energies of the band heads, and

$$\chi(I,0) = 1,\ \chi(I,1) = \left[1 - \frac{2}{I(I+1)}\right]^{1/2} \tag{14}$$

The complete energy of a state is found by solving the Schrödinger equation for the nuclear Hamiltonian of Equation (12). It is equal to

$$E_\nu(I) = E_{rot}(I) + \varepsilon_\nu(I) \tag{15}$$

where $E_{rot}(I)$ is the energy of the rotational core and $\varepsilon_\nu(I)$ is the eigenenergy corresponding to the second term of the Hamiltonian of Equation (12) [28] (a detailed description of the model's Hamiltonian, eigenfunctions, and eigenenergies can be found in Refs. [28–30]). The rotational core energy, $E_{rot}(I)$, agrees with the ground-state energy of the rotational bands in even–even deformed nuclei at the lower values of spin I [29].

For the rotational core, an effective value of the rotational frequency can be determined from the available experimental data using the classical definition of the rotational frequency

$$\omega = \frac{dE}{dI} \tag{16}$$

giving [46]

$$\omega_{eff} = \frac{E^{exp.}(I) - E^{exp.}(I-2)}{\sqrt{I(I+1)} - \sqrt{(I-1)(I-2)}} \tag{17}$$

which, for higher levels of spin I, reduces to [29,46]

$$\omega_{eff} = \frac{E^{exp.}(I) - E^{exp.}(I-2)}{2} \tag{18}$$

Hence, the effective moment of inertia becomes

$$\mathcal{J}_{eff} = \frac{d\sqrt{I(I+1)}}{d\omega_{eff}} \tag{19}$$

From Equations (17) and (19), we calculate the effective rotational frequency ω_{eff} and effective moment of inertia $\mathcal{J}_{eff}$, respectively. For low rotational frequencies, i.e., at low spin values $I \lesssim 8\hbar$, $\mathcal{J}_{eff}$ depends almost linearly on ω_{eff}^2 so we can write

$$\mathcal{J}_{eff} = \mathcal{J}_0 + \mathcal{J}_1\omega_{eff}^2 \tag{20}$$

where $\mathcal{J}_0$ and $\mathcal{J}_1$ are the inertial parameters of the rotational core, determined by the least-squares fit in Equation (20).

Having determined the inertial parameters $\mathcal{J}_0$, $\mathcal{J}_1$, we can employ the Harris parameterization for the calculation of the energy of the rotational ground-state band [47]:

$$E_{rot}(I) = \frac{1}{2}\mathcal{J}_0\omega_{rot}^2(I) + \frac{3}{4}\mathcal{J}_1\omega_{rot}^4(I) \tag{21}$$

$$\tilde{I} \equiv \sqrt{I(I+1)} = \mathcal{J}_0\omega_{rot}(I) + \mathcal{J}_1\omega_{rot}^3(I) \tag{22}$$

where ω_{rot} is the rotational angular frequency of the nuclei defined by the real root of the cubic Equation (22) [28,29]:

$$
\begin{aligned}
\omega_{rot}(I) = & \left\{ \frac{\widetilde{I}}{2\mathcal{J}_1} + \left[\left(\frac{\mathcal{J}_0}{3\mathcal{J}_1} \right)^3 + \left(\frac{\widetilde{I}}{2\mathcal{J}_1} \right)^2 \right]^{1/2} \right\}^{1/3} \\
& + \left\{ \frac{\widetilde{I}}{2\mathcal{J}_1} - \left[\left(\frac{\mathcal{J}_0}{3\mathcal{J}_1} \right)^3 + \left(\frac{\widetilde{I}}{2\mathcal{J}_1} \right)^2 \right]^{1/2} \right\}^{1/3}
\end{aligned} \tag{23}
$$

In the present work, we calculate ω_{eff} and $\mathcal{J}_{eff}$ from Equations (17) and (19) for the first low-lying levels (up to $I = 8^+$) of the g.s. band of the even–even $^{162–184}$Hf isotopes. A linear least-squares fit of Equation (20) is then performed to the aforementioned quantities in order to obtain the values of $\mathcal{J}_0$, $\mathcal{J}_1$, which are presented in Table 1. Based on these values and Equation (21), we proceed to calculate the energies for the $I = 0_1^+, \ldots 20_1^+$ states and compare them with the available experimental data [4]. These are shown in Table 2. Regarding $\mathcal{J}_0$, it increases as the number of nucleons grows, exhibiting a maximum at the middle of the shell ($A = 176$). For isotopes $^{166–172}$Hf, the values of $\mathcal{J}_0$, $\mathcal{J}_1$ calculated in this work are in good agreement with those in the earlier work of Ref. [47].

Table 1. $\mathcal{J}_0$, $\mathcal{J}_1$ values obtained within the framework of the phenomenological model for $^{162–184}$Hf (see text for details). A comparison of the experimental $E(2_1^+)$ values of Ref. [23] and the corresponding values calculated within the framework of the phenomenological model (PhM) is also shown.

Isotope ($Z = 72$)	$\mathcal{J}_0$ **[$\times 10^{-2}$ keV^{-1} $\hbar^{-2}$]**	$\mathcal{J}_1$ **[$\times 10^{-8}$ keV^{-3} $\hbar^{-4}$]**	**$E^{th.}(2_1^+)$ [keV]**	**$E^{exp.}(2_1^+)$ [keV]**
^{162}Hf	0.880	13.804	262.249	285.000
^{164}Hf	1.327	14.623	199.610	210.700
^{166}Hf	1.821	17.266	153.912	158.640
^{168}Hf	2.373	17.522	122.068	124.100
^{170}Hf	2.933	20.097	100.055	100.800
^{172}Hf	3.128	12.837	94.750	95.220
^{174}Hf	3.276	11.366	90.728	90.985
^{176}Hf	3.381	8.958	88.126	88.349
^{178}Hf	3.206	6.822	93.019	93.180
^{180}Hf	3.211	3.584	93.137	93.324
^{182}Hf	3.063	4.440	97.485	97.790
^{184}Hf	2.800	5.465	106.349	107.100

Figures 1 and 2 show the dependence of the moment of inertia, $\mathcal{J}$, (determined through the known relation $2\mathcal{J} = (4I-2)/(E_I - E_{I-2})$ [48], with $E = E^{exp}, E^{th}$ for the experimental and theoretical moments of inertia, respectively) on the squared angular frequency of rotation ω^2 (calculated using Equation (18) for $E = E^{exp}, E^{th}$, as in the case of $\mathcal{J}$). The treatment with the phenomenological model leads to a centrifugal stretching of the nucleus and an increase in $\mathcal{J}$ with the rotational frequency. This increase is almost linear for the lower values of spin (i.e., for $I \lesssim 10\hbar$). For high spin values, the emerging nonlinearity is associated with the mixture of the ground-state band with other rotational bands and with the decrease in nucleon pairing. Similar results are presented in Ref. [49], where the cranked shell model Hamiltonian with pairing correlations, treated by the particle-conserving method (PNC–CSM), is employed to investigate the upbending of the experimental moments of inertia appearing in the neutron-rich $^{170–184}$Hf isotopes.

Table 2. Level energies (in MeV) and rotational frequencies ω_{rot}^{th} (in MeV $\hbar^{-1}$) for the even–even $^{162-184}$Hf isotopes calculated in the framework of the phenomenological model (PhM) using Equations (20) and (23), with the $\mathcal{J}_0$, $\mathcal{J}_1$ values determined in this work (see Table 1). The $E^{exp.}$ values are taken from Refs. [4,23].

Isotope		^{162}**Hf**			^{164}**Hf**			^{166}**Hf**	
I	$E^{exp.}$	E^{th}	ω_{rot}^{th}	$E^{exp.}$	E^{th}	ω_{rot}^{th}	$E^{exp.}$	E^{th}	ω_{rot}^{th}
2_1^+	0.285	0.262	0.183	0.211	0.200	0.148	0.158	0.154	0.119
4_1^+	0.730	0.709	0.253	0.587	0.577	0.220	0.470	0.465	0.185
6_1^+	1.293	1.269	0.302	1.085	1.072	0.270	0.897	0.889	0.234
8_1^+	1.940	1.915	0.341	1.669	1.655	0.310	1.406	1.398	0.273
10_1^+	2.635	2.632	0.374	2.304	2.311	0.344	1.972	1.978	0.306
12_1^+	3.185	3.409	0.402	2.995	3.028	0.372	2.566	2.619	0.334
14_1^+	3.567	4.239	0.427	3.618	3.799	0.398	—	3.312	0.359
16_1^+	4.068	5.116	0.450	—	4.619	0.421	—	4.053	0.381
18_1^+	4.653	6.036	0.470	—	5.482	0.442	—	4.836	0.402
20_1^+	5.310	6.996	0.489	—	6.386	0.461	—	5.658	0.421
Isotope		^{168}**Hf**			^{170}**Hf**			^{172}**Hf**	
I	$E^{exp.}$	E^{th}	ω_{rot}^{th}	$E^{exp.}$	E^{th}	ω_{rot}^{th}	$E^{exp.}$	E^{th}	ω_{rot}^{th}
2_1^+	0.124	0.122	0.097	0.101	0.100	0.080	0.095	0.095	0.076
4_1^+	0.386	0.383	0.159	0.322	0.320	0.135	0.309	0.308	0.133
6_1^+	0.757	0.753	0.207	0.643	0.639	0.181	0.628	0.626	0.182
8_1^+	1.214	1.209	0.247	1.043	1.039	0.218	1.037	1.035	0.225
10_1^+	1.736	1.737	0.280	1.504	1.509	0.250	1.521	1.523	0.262
12_1^+	2.306	2.327	0.309	2.016	2.039	0.278	2.064	2.080	0.294
14_1^+	2.858	2.971	0.334	2.567	2.621	0.303	2.654	2.700	0.324
16_1^+	3.310	3.664	0.358	3.151	3.251	0.326	3.277	3.375	0.351
18_1^+	3.833	4.401	0.379	3.768	3.923	0.346	3.919	4.101	0.375
20_1^+	4.440	5.178	0.398	4.421	4.635	0.365	4.576	4.874	0.397
Isotope		^{174}**Hf**			^{176}**Hf**			^{178}**Hf**	
I	$E^{exp.}$	E^{th}	ω_{rot}^{th}	$E^{exp.}$	E^{th}	ω_{rot}^{th}	$E^{exp.}$	E^{th}	ω_{rot}^{th}
2_1^+	0.091	0.091	0.073	0.088	0.088	0.071	0.093	0.093	0.075
4_1^+	0.297	0.296	0.129	0.290	0.289	0.127	0.307	0.306	0.134
6_1^+	0.608	0.606	0.178	0.597	0.595	0.177	0.632	0.631	0.188
8_1^+	1.010	1.008	0.221	0.998	0.996	0.222	1.059	1.057	0.237
10_1^+	1.486	1.490	0.260	1.481	1.482	0.262	1.570	1.575	0.280
12_1^+	2.021	2.044	0.294	2.035	2.044	0.299	2.150	2.177	0.320
14_1^+	2.598	2.663	0.324	2.647	2.676	0.332	2.778	2.854	0.356
16_1^+	3.209	3.340	0.352	3.308	3.370	0.362	3.435	3.600	0.389
18_1^+	3.857	4.070	0.378	4.011	4.123	0.390	4.119	4.409	0.420
20_1^+	4.551	4.850	0.401	—	4.929	0.416	4.837	5.277	0.448
Isotope		^{180}**Hf**			^{182}**Hf**			^{184}**Hf**	
I	$E^{exp.}$	E^{th}	ω_{rot}^{th}	$E^{exp.}$	E^{th}	ω_{rot}^{th}	$E^{exp.}$	E^{th}	ω_{rot}^{th}
2_1^+	0.093	0.093	0.076	0.098	0.097	0.079	0.107	0.106	0.086
4_1^+	0.309	0.308	0.136	0.322	0.322	0.142	0.350	0.349	0.153
6_1^+	0.641	0.640	0.194	0.666	0.666	0.200	0.717	0.717	0.213
8_1^+	1.084	1.083	0.247	1.122	1.121	0.253	1.200	1.198	0.266
10_1^+	1.631	1.629	0.297	1.680	1.678	0.302	—	1.780	0.314
12_1^+	2.274	2.271	0.344	2.332	2.329	0.347	—	2.452	0.357
14_1^+	3.005	3.003	0.387	3.065	3.065	0.388	—	3.207	0.396
16_1^+	3.814	3.817	0.427	3.869	3.881	0.426	—	4.036	0.432
18_1^+	4.682	4.709	0.464	4.734	4.769	0.461	—	4.933	0.465
20_1^+	5.554	5.674	0.499	—	5.725	0.494	—	5.893	0.495

A more in-depth consideration of the phenomenological model would require us to consider the eigenfunctions of the Hamiltonian (12), which contain the mixing amplitudes of the various underlying states, for the calculation of the $B(E2)\uparrow$ values. However, in our simplified approach to this model, we instead calculated the $\tau(2_1^+)$ lifetimes, the $B(E2)\uparrow$ values, and the β_2 deformation parameters using the Global Best Fit of Raman et al. [21] from Equations (9)–(11), using the theoretical $E(2_1^+)$ energies resulting from the phenomenological model. The rest of the observables (Q_0, Q, and β_2/β_{SP}) were then calculated with Equations (1), (2), and (5). The results are presented in Tables 3 and 4 and plotted in Figure 3.

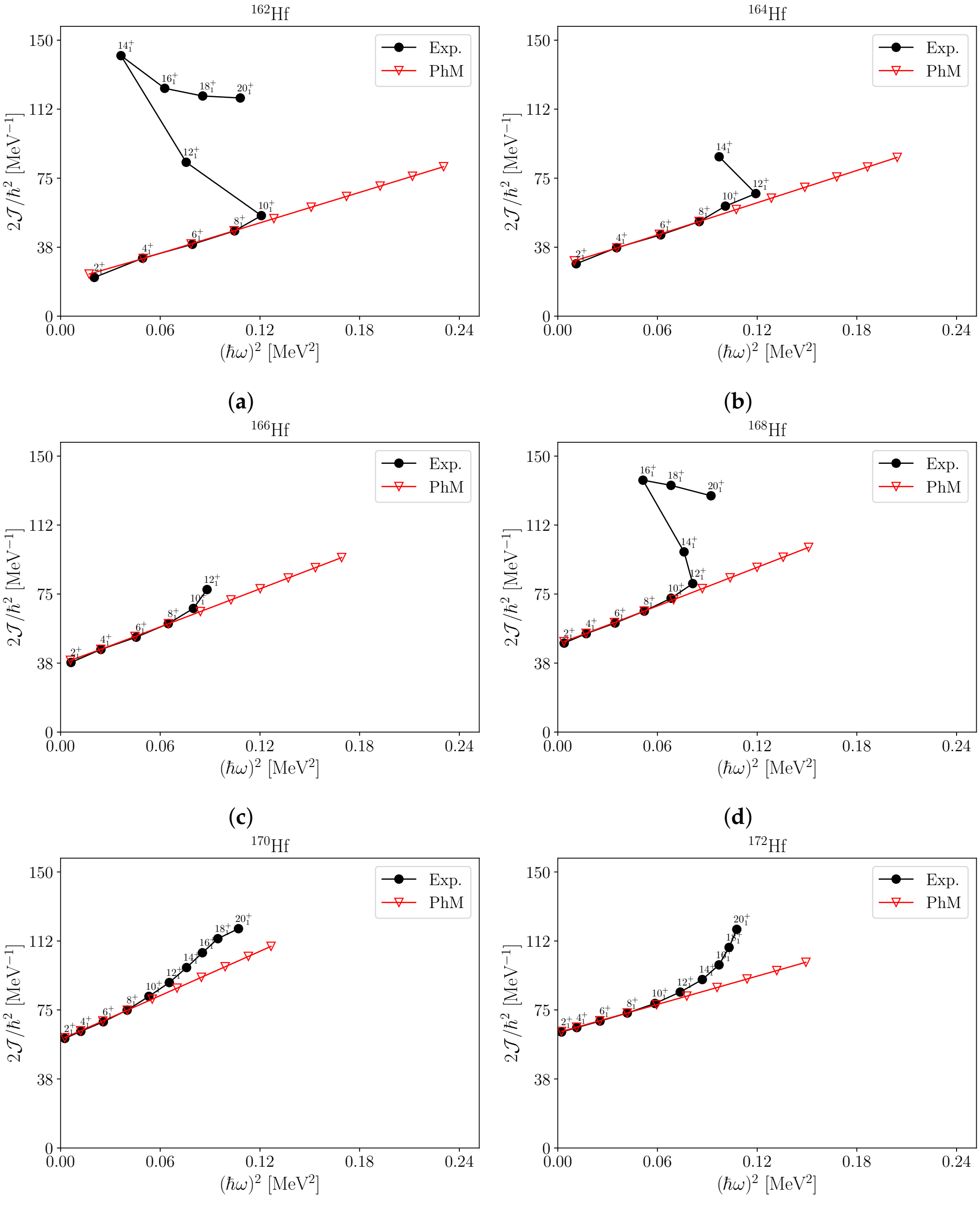

(a) **(b)**

(c) **(d)**

(e) **(f)**

Figure 1. Experimental vs. phenomenological model moments of inertia, $2\mathcal{J} = (4I-2)/(E_I - E_{I-2})$, plotted against the squared angular frequencies of rotation $\omega^2 = (E_I - E_{I-2})^2/4$ [48] for the even–even $^{162\text{–}172}$Hf isotopes: (**a**) ^{162}Hf, (**b**) ^{164}Hf, (**c**) ^{165}Hf, (**d**) ^{168}Hf, (**e**) ^{170}Hf, (**f**) ^{172}Hf. Solid lines are drawn to guide the eye. Experimental uncertainties are smaller than the data symbols.

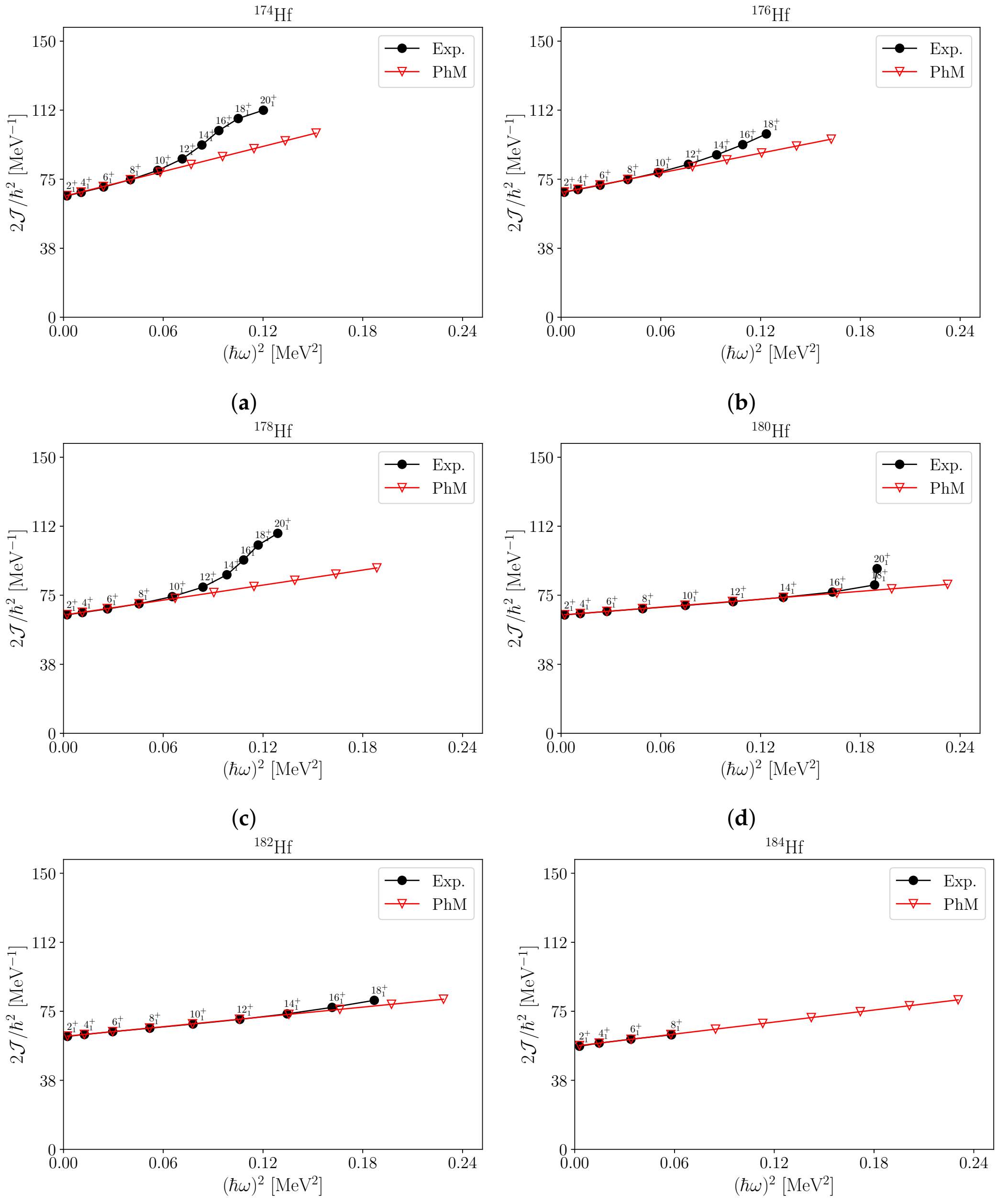

(**a**) (**b**)

(**c**) (**d**)

(**e**) (**f**)

Figure 2. Same as in Figure 1 for the even–even $^{174-184}$Hf isotopes: (**a**) ^{174}Hf, (**b**) ^{176}Hf, (**c**) ^{178}Hf, (**d**) ^{180}Hf, (**e**) ^{182}Hf, (**f**) ^{184}Hf.

3.2. Finite-Range Droplet Model (FRDM)

The finite-range droplet model (FRDM) is a global microscopic–macroscopic model of nuclear structure, which was introduced in 1988 [50], and soon incorporated improvements based on the AME1989 mass evaluation (FRDM92) [51]. The latest enhancement (FRDM12) [52] included adjustments due to the AME2003 mass evaluation (see Figure 1 in Ref. [52]). For our calculations, we use FRDM12 (hereafter referred to as FRDM in Figures and Tables).

In the macroscopic–microscopic method, the total nuclear potential energy, calculated as a function of shape, Z and N, can be expressed as the sum of a microscopic and a macroscopic term. The microscopic terms represent the shell-plus-pairing correction [52], namely

$$E_{pot}(Z,N,shape) = E_{mac}(Z,N,shape) + E_{s+p}(Z,N,shape) \quad (24)$$

The *finite-range droplet model*, an improved version of the *droplet* model [53], is employed for the calculation of the macroscopic contribution of Equation (24). For the microscopic part, proton/neutron shell and pairing corrections have to be taken into account. The matrix elements of the single-particle Hamiltonian are generated from the basis of the axial-symmetric harmonic-oscillator eigenfunctions. The shell correction is carried out using Strutinsky's method [54], whereas for the pairing correction, the Lipkin–Nogami [55,56] version of the Bardeen–Cooper–Schrieffer (BCS) method is employed, which takes into account in lowest order the effects associated with particle number fluctuations and restores approximately the violation of the particle number that occurs in the BCS. A folded Yukawa single-particle potential is assumed in both cases and a zero-point energy is added to the calculated potential energy at the ground-state shape.

This version of the FRDM (FRDM12) allows for the calculation of several nuclear properties in addition to the nuclear ground-state masses. Among these are the ground-state deformation multipoles, calculated through the minimization of the nuclear potential energy function with respect to the parameters ε_2, ε_3, ε_4, and ε_6, as these are defined in the perturbed spheroid parameterization by Nilsson [57]. The β–shape parameters can then be derived using the relation

$$\beta_{lm} = \sqrt{4\pi}\frac{\int r(\theta,\phi)Y_m^l(\theta,\phi)\,d\Omega}{\int r(\theta,\phi)Y_0^0(\theta,\phi)\,d\Omega} \tag{25}$$

with the radius vector r expressed in the ε parametrization [52].

In this work, we used the values for the deformation parameters β_2 and β_4 given in Ref. [52] to calculate the intrinsic quadrupole moments for the 2_1^+ state in even–even $^{162-184}$Hf isotopes using the relation [52]

$$Q_0 = \frac{3ZR_0^2}{\sqrt{5\pi}}\left(\beta_2 + \frac{2}{7}\sqrt{\frac{5}{\pi}}\beta_2^2 + \frac{20}{77}\sqrt{\frac{5}{\pi}}\beta_4^2 + \frac{12}{7\sqrt{\pi}}\beta_2\beta_4\right) + \mathcal{O}(\beta^3) \tag{26}$$

The above derivation requires Q_0 to assume the original value of the considered model when the protons are distributed uniformly inside a liquid drop with a radius R_0 and deformations β_2, β_4 (sharp-edged density model).

Having calculated the intrinsic electric quadrupole moments, the $B(E2)\uparrow$ values can be deduced using Equation (1). The rest of the calculated quantities are obtained using Equations (2), (5) and (6). All the quantities are shown in Tables 3 and 4 and plotted in Figure 3a–f.

3.3. Hartree–Fock BCS with Skyrme MSk7 Model (HFBCS–MSk7)

In the HFBCS–MSk7 model, the nuclear ground-state properties can be deduced using the conventional HF+BCS model coupled with the Skyrme forces [58,59]. In this framework, the ground-state wavefunction is expressed as an expansion of the single-particle wavefunctions in a harmonic-oscillator basis. In addition, a 10-parameter Skyrme interaction (MSk7) is employed, along with a 2-parameter Wigner interaction and a 4-parameter δ-function pairing force. The Skyrme and pairing parameters for the MSk7 force are determined in Ref. [59] by fitting to the same dataset of nuclear masses as its predecessor, the MSk6 force. These parameters are listed in Table A in Ref. [59].

For the case of deformed nuclei (see Ref. [59] for more details), the ETFSI-2 method [60] (where ETFSI stands for *extended Thomas–Fermi plus Strutinsky integral*) is implemented to derive the deformation parameters, which are subsequently used as a starting point in the deformed HF calculations [58]. A correction is made for the spurious center-of-mass motion and the spurious rotational energy of deformed nuclei is subtracted from the total computed amount of energy, as calculated in Ref. [58].

The Skyrme part of the MSk7 force on which the HFBCS-1 table of the different quantities in Ref. [59] is based has the usual form

$$
\begin{aligned}
u_{ij} = &\, t_0(1+x_0P_\sigma)\delta(\vec{r}_{ij}) \\
&+ t_1(1+x_1P_\sigma)\frac{1}{2\hbar^2}\{p_{ij}^2\delta(\vec{r}_{ij})+h.c.\} \\
&+ t_2(1+x_2P_\sigma)\frac{1}{\hbar^2}\vec{p}_{ij}\cdot\delta(\vec{r}_{ij})\vec{p}_{ij} \\
&+ \frac{1}{6}t_3(1+x_3P_\sigma)\rho^\gamma\delta(\vec{r}_{ij}) \\
&+ \frac{i}{\hbar^2}W_0(\vec{\sigma}_i+\vec{\sigma}_j)\cdot\vec{p}_{ij}\times\delta(\vec{r}_{ij})\vec{p}_{ij}
\end{aligned}
\tag{27}
$$

In the above equation, P_σ is the two-body spin-exchange operator, whereas the δ-function pairing force can be expressed as [59]

$$v_{pair}(r_{ij}) = V_{\pi q}\delta(r_{ij}) \tag{28}$$

where the pairing-strength parameter $V_{\pi q}$ receives different values for protons and neutrons, whereas it is slightly stronger for odd nucleons ($V_{\pi q}^-$) than for even nucleons ($V_{\pi q}^+$) (see Ref. [58] for more details). As for the Wigner correction term, it has the form

$$E_W = V_W e^{-\lambda/N-Z/A} \tag{29}$$

The Skyrme pairing $V_{\pi q}^+$, $V_{\pi q}^-$ and Wigner parameters V_W and λ are determined via a fit on the 1995 mass compilation (Audi and Wapstra). The rather standard HF–MSk7 formalism is summarized in Ref. [58].

Using the β_2 and β_4 deformation parameter values obtained from the HFBCS-1 table in Ref. [59], we proceed to calculate the intrinsic quadrupole deformation Q_0 for the even–even $^{162-184}$Hf isotopes using Equation (26). The rest of the physical quantities studied in this work are subsequently deduced from Equations (1), (2), (5) and (6). The results are shown in Tables 3 and 4 and plotted in Figure 3a–f.

3.4. Hartree–Fock–Bogoliubov with Gogny D1S interaction (HFB–Gogny D1S)

The microscopic Hartree–Fock–Bogoliubov (HFB) method with the Gogny D1S effective nucleon–nucleon interaction [61,62] is a powerful approach with good predictive power in various aspects of nuclear structure [63]. Incorporating the mean-field approach, a many-body, effective Hamiltonian for the nucleus is expressed as

$$H = \sum_i^A T_i + \frac{1}{2}\sum_{i\neq j}^A u_{ij} \tag{30}$$

with T_i being the kinetic energy of the nucleon i and u_{ij} being the Gogny effective nucleon–nucleon interaction. The D1S parameterization of the Gogny force (Gogny D1S) [62]—a widely tested effective interaction—is used in the works of Refs. [63,64] to calculate various nuclear properties, among which are the β_2 ground-state deformation parameters.

Here, we give a brief description of the HFB–Gogny D1S model. Due to its finite range, the D1S interaction can be used in the framework of the full Hartree–Fock–Bogoliubov theory (HFB) to generate the nuclear pairing field in addition to the nuclear mean field [61], which gives it an advantage over the Skyrme interaction. The D1S effective nucleon–nucleon interaction is parameterized as

$$\begin{aligned} u_{12} = & \sum_{j=1}^{2} \exp\left[-\frac{(\vec{r}_1-\vec{r}_2)^2}{\mu_j^2}\right] \times (W_j + B_j P_\sigma - H_j P_\tau - M_j P_\sigma P_\tau) \\ & + t_3(1+x_0 P_\sigma)\delta(\vec{r}_1-\vec{r}_2)\left[\rho\left(\frac{\vec{r}_1+\vec{r}_2}{2}\right)\right]^a \\ & + iW_{LS}\overleftarrow{\nabla}_{12}\delta(\vec{r}_1-\vec{r}_2)\times\overrightarrow{\nabla}_{12}\cdot(\vec{\sigma}_1+\vec{\sigma}_2) \\ & + (1+2\tau_{1z})(1+2\tau_{2z})\frac{e^2}{|\vec{r}_1-\vec{r}_2|} \end{aligned} \tag{31}$$

In the above expression, the first term includes two finite ranges and the common mixing of spin, isospin, and space exchange operators (P_σ, P_τ and $-P_\sigma P_\tau$, respectively). A functional of the nuclear density ρ is the second term; a zero-range, two-body spin-orbit interaction is the third term; and the Coulomb repulsion among protons is the fourth term.

For the self-consistent solution of the HFB equations [64,65], an iterative method is employed that is based on the minimization of the total energy of the nucleus

$$\delta\Big(\langle\Phi|(H-\lambda_2 Q_{20}-\lambda_Z Z-\lambda_N N)|\Phi\rangle\Big) = 0 \tag{32}$$

In this expression:

1. H is the nuclear Hamiltonian of Equation (30).
2. $|\Phi\rangle$ is the HFB wavefunction.
3. λ_Z, λ_N are the Lagrange parameters fixing the proton and neutron numbers, respectively.
4. λ_2 is the Lagrange parameter to fix the quadrupole moment q_{20}, defined as

$$q_{20} = \langle\Phi|Q_{20}|\Phi\rangle \tag{33}$$

with the operator Q_{20}

$$Q_{20} = \sqrt{\frac{16\pi}{5}}r^2 Y_{20} \tag{34}$$

A harmonic-oscillator basis with axial symmetry is used in this approach and the deformation parameters β_2 are given by

$$\beta_2 = \frac{1}{AR^2}\sqrt{\frac{5\pi}{9}}q_{20} \tag{35}$$

In the above equation, $R = 1.2A^{1/3}$ fm is the nuclear radius and q_{20} is the quadrupole moment of Equation (33), expressed in units of fm^2 [63]. The results obtained with the above method are included in the AMEDEE database [64], where large-scale, axial mean-field calculations from the proton to the neutron dripline were carried out.

In the case of the HFB–Gogny D1S model, the deformation parameters β_{min} were obtained from Ref. [64] and used as the β_2 deformation parameters to calculate the quantities shown in Tables 3 and 4 with the help of Equations (1), (2), and (4)–(6). The results are plotted in Figure 3a–f.

3.5. Hatree–Fock–Bogoliubov UNEDF–1 (HFB–UNEDF–1)

In the framework of the Hartree–Fock–Bogoliubov theory, M. Kortelainen et al. [66] proposed a new Skyrme-like energy density functional, UNDEF-1, suitable for the description of nuclei with strong elongation. In the nuclear density functional theory (DFT), the total binding energy E of the nucleus is a functional of the one-body density ρ and the pairing matrices $\tilde{\rho}$. In its quasilocal approximation, it can be expressed as a three-dimensional (3D) spatial integral [66]:

$$
\begin{aligned}
E[\rho,\tilde{\rho}] &= \int d^3\vec{r}\mathcal{H}(\vec{r}) \\
&= \int d^3\vec{r}\big[\mathcal{E}^{kin}(\vec{r}) + \chi_0(\vec{r}) + \chi_1(\vec{r}) \\
&\quad + \tilde{\chi}(\vec{r}) + \mathcal{E}^{Coul}_{Dir}(\vec{r}) + \mathcal{E}^{Coul}_{Exc}(\vec{r})\big]
\end{aligned} \tag{36}
$$

where $\mathcal{H}(\vec{r})$ is the energy density, which is quasilocal, time-even, scalar, isoscalar, and real. It is usually broken down into the kinetic energy $\mathcal{E}^{kin}(\vec{r})$; isoscalar and isovector particle-hole energy densities $\chi_i(\vec{r})$, $i = 0, 1$; pairing energy $\chi(\vec{r})$; and Coulomb terms ($\mathcal{E}^{Coul}_{Dir}(\vec{r})$, $\mathcal{E}^{Coul}_{Exc}(\vec{r})$). We will not present here the full theoretical framework related to UNEDF-1 but refer the reader to Ref. [66] and the references therein. The results were obtained using the solver HFBTHO in the axial-symmetric harmonic-oscillator basis and the Lipkin–Nogami version of the BCS theory. These results, which are available on the Mass Explorer [67] website, were obtained with large-scale DFT calculations focusing on the ground-state properties of even–even nuclei across the nuclear chart.

In this work, we use the β_2 deformation parameters obtained from the HFB formalism with the UNEDF-1 energy density functional [67] to calculate the quantities shown in Tables 3 and 4 using Equations (1), (2), and (4)–(6). The results are plotted in Figure 3a–f.

3.6. Relativistic Hartree–Bogoliubov Covariant Energy Density Functional NL3* (RHB–NL3*)

Density functional theory has proven to be a universal and powerful tool in nuclear structure theory, showing great success in the description of various nuclear phenomena spanning the full range of the periodic table [68]. The form of DFT is determined by symmetry arguments and simplicity. The remaining parameter sets are deduced by fitting them to the experimental data. The relativistic (covariant) DFTs (CDFTs) provide some of the most interesting cases among the existing nuclear DFTs, respecting the Lorentz covariance while taking advantage of the basic properties of QCD at low energies such as symmetries and separation of scales. In this work, we consider the large-scale axial relativistic Hartree–Bogoliubov calculations of Abgemava et al. [69,70] and employ the covariant density functional NL3* [71], a nonlinear nucleon–meson coupling model.

Relativistic mean-field (RMF) theory [72], which is based on the Walecka model [73,74], is the starting point in the development of a covariant density functional (CDF). In this model, the exchange of phenomenological mesons drives the interaction of nucleons. In all the CDFs developed so far, two assumptions have been essential [75,76]: (i) the *mean-field approximation* in which only the nucleonic fields are quantized and the nucleons move independently in classical meson fields depending on the nuclear densities and currents in a self-consistent way and (ii) the *no-sea approximation* in which vacuum polarization and the contributions arising from the negative energy solutions are not explicitly taken into account.

The starting point of the NL3* CDFT is a standard Lagrangian density of the form

$$
\begin{aligned}
\mathcal{L} = &\bar{\psi}[\gamma(i\partial - g_\omega\omega - g_\rho\vec{\rho}\vec{\tau} - eA) - m - g_\sigma\sigma]\psi \\
&+ \frac{1}{2}(\partial\sigma)^2 - \frac{1}{2}m_\sigma^2\sigma^2 - \frac{1}{4}\Omega_{\mu\nu}\Omega^{\mu\nu} + \frac{1}{2}m_\omega^2\omega^2 \\
&- \frac{1}{4}\vec{R}_{\mu\nu}\vec{R}^{\mu\nu} + \frac{1}{2}m_\rho^2\vec{\rho}^2 - \frac{1}{4}F_{\mu\nu}F^{\mu\nu}
\end{aligned} \tag{37}
$$

containing nucleons of mass m described by the Dirac spinors ψ and various relativistic fields characterized by the spin, parity, and isospin quantum numbers. These are effective fields that are mediated by mesons characterizing the properties of the possible relativistic fields in the effective Dirac equation. The latter corresponds to the Kohn–Sham equation (KS) in the non-relativistic case. It is only for simplicity that the conventional names $\sigma(I^\pi = 0^+, T = 0)$, $\omega(I^\pi = 1^-, T = 0)$ and $\rho(I^\pi = 1^-, T = 1)$ are used. The electromagnetic field A is also included in the above expression [75] (for a more detailed definition and description of the various quantities used in the above Lagrangian, see Ref. [72]).

Table 3. Values of the reduced transition matrix elements $B(E2; 0_1^+ \to 2_1^+)$ and the lifetimes $\tau(2_1^+)$ (see text for more details about the relevant calculations). The results are compared with the experimental values [4,22,23]. Predictions for isotopes ^{182,184}Hf, for which no experimental data exist, are denoted in bold.

Isotope	**Exp.**	**Global Fit**	**PhM**	**FRDM**	**HFBCS–MSk7**	**HFB–Gogny D1S**	**HFB–UNEDF–1**	**RHB–NL3***
$B(E2; 0_1^+ \to 2_1^+)$ [e^2 b^2]								
^{162}Hf	1.34(10)	1.6(3)	1.710	2.109	2.230	2.208	2.287	2.143
^{164}Hf	1.82(17)	2.1(4)	2.228	2.774	3.046	3.383	2.953	2.809
^{166}Hf	$3.46^{+0.17}_{-0.15}$	2.8(5)	2.866	3.452	3.407	4.766	3.744	3.692
^{168}Hf	4.393(36)	3.5(6)	3.585	4.240	4.815	5.925	5.118	5.283
^{170}Hf	5.11(18)	4.3(8)	4.339	5.148	5.719	6.514	6.138	6.132
^{172}Hf	5.77(10)	4.5(8)	4.546	5.172	6.257	6.935	6.511	6.421
^{174}Hf	5.38(20)	4.7(8)	4.711	5.592	7.086	7.002	6.480	6.132
^{176}Hf	5.42(17)	4.8(8)	4.814	5.138	5.364	6.620	5.967	5.695
^{178}Hf	4.736(63)	4.5(8)	4.526	5.103	4.633	6.087	5.145	5.375
^{180}Hf	4.6470(30)	4.5(8)	4.487	4.638	3.333	5.567	4.656	5.093
^{182}Hf	—	**4.2(7)**	**4.255**	**4.656**	**3.949**	**5.061**	**4.332**	**4.813**
^{184}Hf	—	**3.8(7)**	**3.872**	**4.191**	**4.376**	**4.435**	**3.934**	**4.401**
$\tau(2_1^+)$ [ps]								
^{162}Hf	148(11)	126(22)	176	94	89	90	87	93
^{164}Hf	435(41)	376(66)	467	286	261	235	269	283
^{166}Hf	717(33)	895(157)	1010	721	731	522	665	674
^{168}Hf	1239(10)	1548(271)	1654	1287	1134	921	1067	1033
^{170}Hf	1740(61)	2074(363)	2137	1735	1562	1371	1455	1457
^{172}Hf	1710^{+31}_{-39}	2199(385)	2243	1924	1590	1435	1528	1550
^{174}Hf	1986^{+77}_{-71}	2291(401)	2317	1925	1519	1537	1661	1755
^{176}Hf	2069^{+67}_{-63}	2350(411)	2373	2196	2103	1704	1891	1981
^{178}Hf	2168(29)	2288(401)	2304	2026	2231	1698	2009	1923
^{180}Hf	2203.9(14)	2303(403)	2322	2224	3094	1853	2215	2025
^{182}Hf	—	**2236(392)**	**2265**	**2038**	**2403**	**1875**	**2190**	**1971**
^{184}Hf	—	**2063(376)**	**2122**	**1893**	**1813**	**1789**	**2017**	**1803**

The meson masses m_σ, m_ω, and m_ρ and the respective coupling constants g_σ, g_ω, and g_ρ are entered into the Lagrangian of Equation (37), which was first introduced by Walecka [73,74]. This model, however, was unsuccessful in accurately describing the surface properties of finite nuclei and, in particular, the incompressibility. Therefore, in Ref. [77] Boguta and Bodmer introduced an additional density dependence using a nonlinear meson coupling. In that scheme, the $\frac{1}{2}m_\sigma^2\sigma^2$ term in Equation (37) was replaced with

$$U(\sigma) = \frac{1}{2}m_\sigma^2\sigma^2 + \frac{1}{3}g_2\sigma^3 + \frac{1}{4}g_3\sigma^4 \tag{38}$$

The NL3* parameter fit leads to a good description of nuclear masses, simultaneously providing good results for the collective properties of the rotational and vibrational character [69,70,75]. The parameters of NL3*, along with their values, are given in Refs. [70,75].

Following a similar path to the case of the HFB–Gogny D1S model, we proceed to calculate the various observables. The starting point for our calculations is the β_2 deformation parameters obtained from Ref. [67] in the framework of the relativistic Hartree–Bogoliubov (RHB) theory using the NL3* covariant energy density functional (labeled RHB–NL3* in the tables and graphs). The results are presented in Tables 3 and 4 and plotted in Figure 3a–f.

Table 4. Values of the β_2/β_{SP} ratios, intrinsic quadrupole moments Q_0, and electric quadrupole moments Q (see text for more details about the relevant calculations). The "experimental" values are calculated from Equations (1), (2), (4), and (5) using the experimental $B(E2)$s of Ref. [23] (see also Table 3). Predictions for isotopes ^{182,184}Hf, for which no experimental data exist, are denoted in bold.

Isotope	"Exp."	Global Fit	PhM	FRDM	HFBCS–MSk7	HFB–Gogny D1S	HFB–UNEDF–1	RHB–NL3*
				β_2/β_{SP}				
^{162}Hf	7.13(27)	7.7(7)	8.044	8.287	8.604	9.147	9.311	9.011
^{164}Hf	8.2(4)	8.9(8)	9.107	9.328	9.962	11.230	10.493	10.234
^{166}Hf	$11.27^{+0.28}_{-0.24}$	10.1(9)	10.247	10.325	10.415	13.223	11.720	11.638
^{168}Hf	12.59(5)	11.3(10)	11.369	11.366	12.226	14.626	13.594	13.811
^{170}Hf	13.48(24)	12.4(11)	12.409	12.408	13.132	15.215	14.770	14.762
^{172}Hf	14.22(14)	12.6(11)	12.604	12.453	13.585	15.577	15.093	14.989
^{174}Hf	13.63(27)	12.7(11)	12.732	13.042	14.491	15.532	14.943	14.536
^{176}Hf	13.54(23)	12.8(11)	12.772	12.589	12.679	14.989	14.230	13.902
^{178}Hf	12.58(8)	12.3(11)	12.292	12.589	11.774	14.264	13.115	13.404
^{180}Hf	12.371(4)	12.1(11)	12.148	12.091	9.962	13.540	12.383	12.951
^{182}Hf	—	**11.7(10)**	**11.743**	**12.136**	**10.868**	**12.815**	**11.856**	**12.498**
^{184}Hf	—	**11.1(10)**	**11.121**	**11.592**	**11.321**	**11.909**	**11.217**	**11.864**
				Q_0 [b]				
^{162}Hf	3.67(27)	4.0(7)	4.146	4.604	4.735	4.711	4.795	4.641
^{164}Hf	4.28(40)	4.6(8)	4.732	5.280	5.534	5.831	5.449	5.314
^{166}Hf	$5.90^{+0.29}_{-0.26}$	5.3(9)	5.368	5.891	5.852	6.922	6.135	6.092
^{168}Hf	6.650(54)	6.0(10)	6.003	6.529	6.958	7.718	7.173	7.288
^{170}Hf	7.17(25)	6.6(12)	6.605	7.194	7.582	8.092	7.856	7.851
^{172}Hf	7.62(13)	6.7(12)	6.761	7.211	7.931	8.350	8.090	8.034
^{174}Hf	7.35(27)	6.9(12)	6.882	7.498	8.440	8.390	8.071	7.852
^{176}Hf	7.38(23)	6.9(12)	6.957	7.187	7.344	8.158	7.745	7.567
^{178}Hf	6.900(92)	6.7(12)	6.746	7.162	6.825	7.823	7.192	7.351
^{180}Hf	6.8300(44)	6.7(12)	6.716	6.828	5.788	7.481	6.842	7.155
^{182}Hf	—	**6.5(11)**	**6.541**	**6.841**	**6.300**	**7.133**	**6.599**	**6.956**
^{184}Hf	—	**6.2(11)**	**6.239**	**6.491**	**6.633**	**6.677**	**6.289**	**6.652**
				Q [b]				
^{162}Hf	−1.05(8)	−1.14(20)	−1.184	−1.316	−1.353	−1.346	−1.370	−1.326
^{164}Hf	−1.22(11)	−1.32(23)	−1.352	−1.509	−1.581	−1.666	−1.557	−1.518
^{166}Hf	$-1.69^{+0.8}_{-0.7}$	−1.51(26)	−1.534	−1.683	−1.672	−1.978	−1.753	−1.741
^{168}Hf	−1.899(16)	−1.7(3)	−1.715	−1.865	−1.988	−2.205	−2.049	−2.082
^{170}Hf	−2.05(7)	−1.9(3)	−1.887	−2.055	−2.166	−2.312	−2.244	−2.243
^{172}Hf	−2.18(4)	−1.9(3)	−1.932	−2.060	−2.266	−2.386	−2.311	−2.295
^{174}Hf	−2.10(8)	−2.0(3)	−1.966	−2.142	−2.411	−-2.397	−2.306	−2.243
^{176}Hf	−2.11(7)	−2.0(3)	−1.988	−2.053	−2.098	−2.331	−2.213	−2.162
^{178}Hf	−1.971(26)	−1.9(3)	−1.927	−2.046	−1.950	−2.235	−2.055	−2.100
^{180}Hf	−1.9528(13)	−1.9(3)	−1.919	−1.951	−1.654	−2.137	−1.955	−2.044
^{182}Hf	—	**−1.9(3)**	**−1.869**	**−1.955**	**−1.800**	**−2.038**	**−1.885**	**−1.988**
^{184}Hf	—	**−1.8(3)**	**−1.783**	**−1.854**	**−1.895**	**−1.908**	**−1.797**	**−1.901**

4. Results and Discussion

The various observables calculated in this work for the even–even $^{162–184}$Hf isotopes with the six different models described in Section 3 are shown in Tables 3 and 4 and plotted in Figure 3a–f. These are compared with existing experimental data and with Raman's Global Best Fit predictions [21]. We should clarify that in the case of the quantities labeled "Exp." in Table 4, the "experimental" values refer to the values resulting from Equations (1), (2), (4), and (5) using the experimental $B(E2)$s of Ref. [23]. We should also mention that experimental data for Q exist for the cases of isotopes ^{176,178,180}Hf [78]. Those values are close to the ones presented in Table 4. All of the theoretical predictions of the models considered in this work seem to be able to reproduce the trend of the experimental data fairly well.

Regarding the energies of the low-lying excited states of the ground-state bands in the even–even $^{162–184}$Hf, the phenomenological model employed in this work led to a very good description of the first low-lying energy levels, yielding an excellent agreement with the experimental values of Refs. [23,43] for the $E(2_1^+)$ levels (see Tables 1 and 2), as well as with the theoretical results in the earlier works of Refs. [28–30,47]. The anti-correlation effect between the $E(2_1^+)$ energies and the deformation parameters β_2 was observed as expected. However, the energy difference $\Delta E(I) = E^{th}(I) - E^{exp}(I)$ presented an increase with the increasing angular momentum I. This is due to the occurrence of the non-adiabaticity of the energy rotational bands in large spin [28,29].

For the $B(E2;0_1^+ \to 2_1^+)$ reduced transition rates, the intrinsic quadrupole moments Q_0 and the electric quadrupole moments Q, the FRDM led to an improved description of the available experimental data compared to the other models considered in this study. The HFB formalism slightly overestimated the Q, Q_0, and $B(E2) \uparrow$ values when the Gogny D1S interaction was used (HFB–Gogny D1S model, green squares in graphs). This behavior seems to improve slightly in the case of the Skyrme-type energy density functional UNEDF-1 (orange triangles in graphs). Similar behavior was observed in the case of the relativistic (covariant) energy density functional NL3* (RHB–NL3*, purple triangles in graphs). The aforementioned models (HFB–Gogny D1S, HFB–UNEDF–1, RHB–NL3*) are based on the HFB formalism, differing in the implementation (nonrelativistic, relativistic) and the effective interactions used. It is interesting that, besides their differences, they exhibited a similar trend of slightly overestimating the Q_0, Q, and $B(E2) \uparrow$ values compared to the experimental data in Ref. [23]. Similar conclusions regarding various quantities were drawn, for instance, in the case of Hg isotopes [79] regarding the comparison of self-consistent Skyrme and Gogny forces and for heavier nuclei in the transactinide region around nobelium regarding the performance of Skyrme, Gogny, and covariant energy density functionals [80].

Regarding the β_2/β_{SP} ratios, the “experimental” values in Table 4 were calculated from the adopted $B(E2) \uparrow$ values of Ref. [23] using the rotational model (Equation (4)). The “experimental” values of Ref. [23] are almost equal to those of Ref. [21], which is to be expected since the $B(E2) \uparrow$ values obtained by Pritychenko et al. and Raman et al. coincided up to the first decimal digit. Nuclear deformations are difficult to determine experimentally; therefore, deducing the deformation values from experimental data is associated with a considerable model dependence. However, the work of Raman and collaborators [20,21] in which Equation (4) was used seems to be the most common pathway for deducing deformations from experiments and conducting a systematic comparison of various model calculations [52]. All of the examined models were successful in reproducing the trend of the “experimental” β_2/β_{SP} ratios (Figure 3b), which were well over unity, revealing the collective quadrupole motion in the neutron-rich even–even Hf isotopes and indicating a correlation between deformation and the filling of major shells. Depending on the model, the maximum deformation was observed in either ^{172}Hf or ^{174}Hf, whereas the maximum value was observed “experimentally” for $A = 172$, four neutrons away from the mid-shell $A = 176$. This differs from the case of the Yb isotopes [37] in which depending on the model, the maximum deformation was observed four or two neurons away from the mid-shell (^{172}Yb or ^{170}Yb) but the “experimental” one was observed two neutrons away from the mid-shell ^{174}Yb. We should note that the β_2 values used to determine the β_2/β_{SP} ratios in this work were taken from the relevant references for each model. Furthermore, it should be stressed that depending on the availability of data, the β_2 values refer to either (i) the quadratic deformation of the mass distribution (for models FRDM, HFB–Gogny–D1S, and HFBCS–MSk7), or (ii) the quadratic deformation of the nuclear charge distribution.

However, in this mass region, the two deformation parameters are expected to differ by less than 5%.

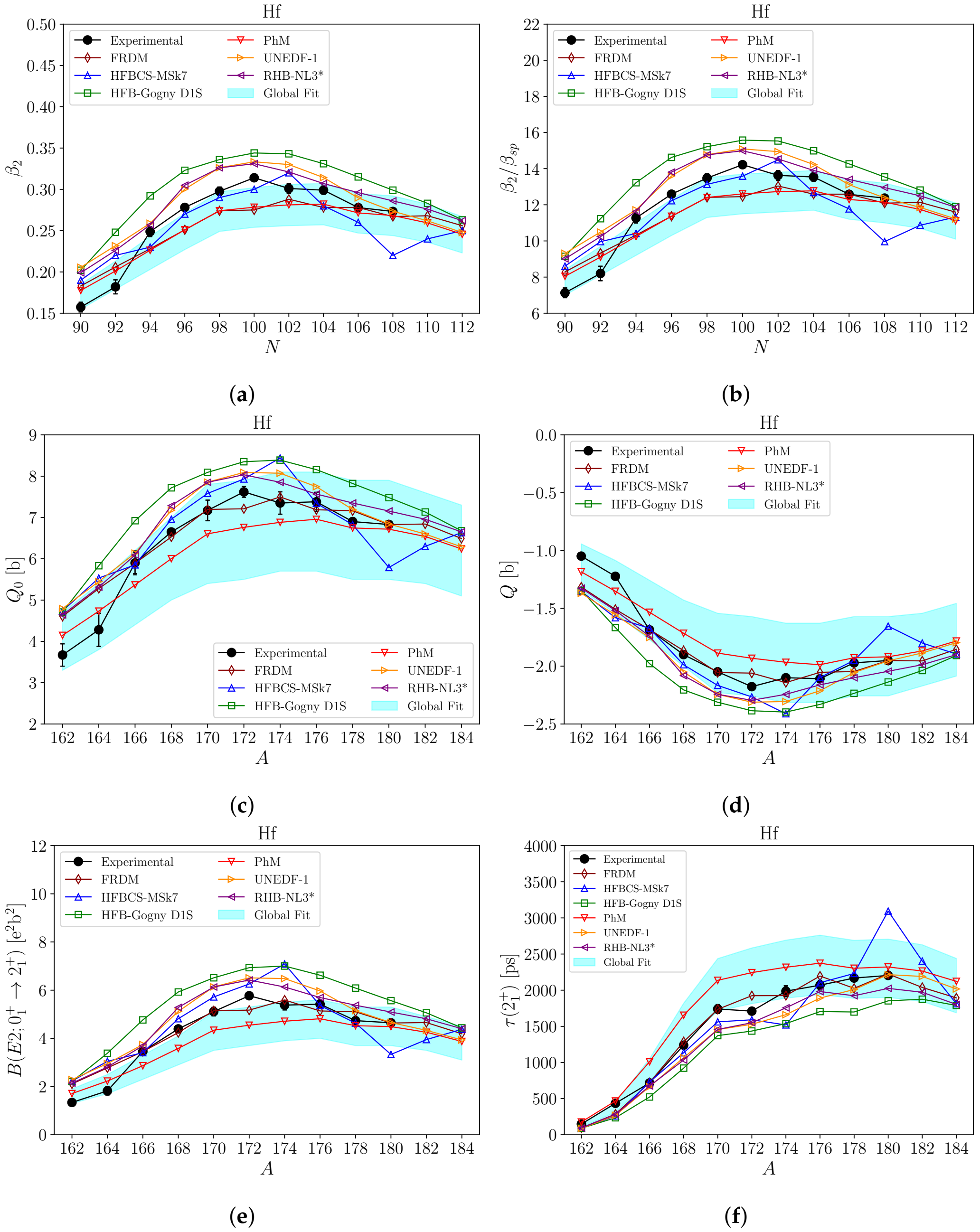

(**a**) (**b**)

(**c**) (**d**)

(**e**) (**f**)

Figure 3. β_2 deformation parameters (**a**), β_2/β_{SP} ratios (**b**), intrinsic Q_0 (**c**) and electric quadrupole moments Q (**d**), $B(E2;0_1^+ \rightarrow 2_1^+)$ reduced electric transition probabilities (**e**), and lifetimes $\tau(2_1^+)$ (**f**) calculated for the even–even $^{162–184}$Hf isotopes using the models presented in Section 3 (for abbreviations, see text). The theoretical predictions are compared with the global fit [21] values (cyan-shaded areas in the graphs), as well as the experimental data where available [4,23].

Based on the good agreement between the theoretical models studied in this work and the experimental data, we attempted to further extend the results to the neutron-rich nuclei ^{182}Hf and ^{184}Hf for which no experimental data other than the $E(2_1^+)$ exist. The predictions regarding the β_2 deformation parameters, β_2/β_{SP} ratios, intrinsic quadrupole moments Q_0 and electric quadrupole moments Q, $B(E2;0_1^+ \rightarrow 2_1^+)$ reduced electric quadrupole transition probabilities, and lifetimes $\tau(2_1^+)$ are presented in Tables 3 and 4 and plotted in Figure 3a–f. It is encouraging that the spread of the values among the different theoretical models for each quantity we examined decreases toward the more neutron-rich isotopes and is smaller than that of the global model, thus reducing the uncertainty of our predictions.

5. Conclusions

In the framework of the collective model, we conclude that the quadrupole moments are successfully calculated for a number of permanently deformed even–even nuclei belonging to the Hf isotopic chain in the rare-earth part of the nuclear chart. A $B(E2; 0_1^+ \rightarrow 2_1^+)$ data compilation was assembled for the even–even $^{162–184}$Hf isotopes using six different models. Based on the deformation parameters β_2, other physical quantities were additionally calculated, providing further insight into the phenomena related to the nuclear symmetries defining the shape of the nucleus. The β_2/β_{SP} ratio is considerably greater than the unity, indicating that these nuclei demonstrate greater quadrupole deformations than would be expected from shell model predictions.

In this context, the sub-shell structure seems to be important. Some theoretical investigations [51,81,82] predict that the maximum quadrupole deformation occurs below $N = 104$ within an isotopic chain, whereas some available experimental data suggest that the deformations increase as the proton number decreases below the mid-shell [83,84]. The strength of the $E2$ transitions between successive levels is of importance for clarifying some ambiguities in the structure of the observed states.

Based on the good agreement between the results of the theoretical models and the experimental data for the $^{162–184}$Hf isotopes, we made predictions for the lifetimes of the 2_1^+ state, the $B(E2; 0_1^+ \rightarrow 2_1^+)$ reduced transition matrix elements, the intrinsic quadrupole moments Q_0, the electric quadrupole moments Q, and the β_2/β_{SP} ratios for isotopes ^{182}Hf and ^{184}Hf (denoted in bold in Tables 3 and 4) for which no information exists other than the energy of the 2_1^+ state. This newly acquired information can serve as a comprehensive guide for current and future experiments focused on neutron-rich hafnium isotopes.

Author Contributions: Conceptualization, P.V., T.J.M. and E.M.; Methodology, P.V., T.J.M. and E.M.; Software, P.V.; Validation, P.V., T.J.M., E.M. and A.Z.; Formal analysis, P.V.; Investigation, P.V.; Writing—original draft preparation, P.V., T.J.M. and E.M.; Writing—review and editing, P.V., T.J.M., E.M. and A.Z.; Visualization, P.V.; Supervision, T.J.M. and E.M. All authors have read and agreed to the published version of the manuscript.

Funding: This research work was supported by the Hellenic Foundation for Research and Innovation (HFRI) under the HFRI Ph.D. Fellowship grant (Fellowship Number: 101742/2019) for AZ.

Institutional Review Board Statement: Not applicable.

Informed Consent Statement: Not applicable.

Data Availability Statement: Not applicable.

Conflicts of Interest: The authors declare no conflict of interest. The funders had no role in the design of the study; in the collection, analysis, or interpretation of data; in the writing of the manuscript; or in the decision to publish the results.

References

1. Drout, M.R.; Piro, A.L.; Shappee, B.J.; Kilpatrick, C.D.; Simon, J.D.; Contreras, C.; Coulter, D.A.; Foley, R.J.; Siebert, M.R.; Morrell, N.; et al. Light curves of the neutron star merger GW170817/SSS17a: Implications for r–process nucleosynthesis. *Science* **2017**, *358*, 1570. [CrossRef] [PubMed]
2. Tarasov, O.B.; Ahn, D.S.; Bazin, D.; Fukuda, N.; Gade, A.; Hausmann, M.; Inabe, N.; Ishikawa, S.; Iwasa, N.; Kawata, K.; et al. Discovery of ^{60}Ca and Implications For the Stability of ^{70}Ca. *Phys. Rev. Lett.* **2018**, *121*, 022501. [CrossRef] [PubMed]
3. Walker, P.; Dracoulis, G. Exotic Isomers in Deformed Atomic Nuclei. *Hyperfine Interact.* **2001**, *135*, 83–107. [CrossRef]
4. National Nuclear Data Center. Available online: https://www.nndc.bnl.gov/nudat2 (accessed on 1 December 2022).
5. Kota, V. Low lying spectra and electromagnetic transitions for ^{164}Dy, ^{166}Er, and ^{168}Yb nuclei. *Phys. Rev. C* **1979**, *19*, 521. [CrossRef]
6. Heyde, K.; Wood, J.L. Shape coexistence in atomic nuclei. *Rev. Mod. Phys.* **2011**, *83*, 1467–1521. [CrossRef]
7. Robledo, L.; Rodríguez-Guzmán, R.; Sarriguren, P. Role of triaxiality in the ground–state shape of neutron–rich Yb, Hf, W, Os and Pt isotopes. *J. Phys. G Nucl. Part. Phys.* **2009**, *36*, 115104. [CrossRef]

8. Nomura, K.; Otsuka, T.; Rodríguez-Guzmán, R.; Robledo, L.; Sarriguren, P. Collective structural evolution in neutron–rich Yb, Hf, W, Os, and Pt isotopes. *Phys. Rev. C* **2011**, *84*, 054316. [CrossRef]
9. Bonatsos, D.; Assimakis, I.; Minkov, N.; Martinou, A.; Sarantopoulou, S.; Cakirli, R.; Casten, R.; Blaum, K. Analytic predictions for nuclear shapes, prolate dominance, and the prolate-oblate shape transition in the proxy–SU(3) model. *Phys. Rev. C* **2017**, *95*, 064326. [CrossRef]
10. Bonatsos, D. Prolate over oblate dominance in deformed nuclei as a consequence of the SU(3) symmetry and the Pauli principle. *Eur. Phys. J. A* **2017**, *53*, 148. [CrossRef]
11. Bohr, A.N.; Mottelson, B.R. *Nuclear Structure*; Vol. II: Nuclear Deformations; World Scientific Publishing: Singapore , 1998.
12. Greiner, W.; Maruhn, J.A. *Nuclear Models*; Springer: Berlin/Heidelberg, Germany, 1996.
13. Ogle, W.; Wahlborn, S.; Piepenbring, R.; Fredriksson, S. Single–Particle Levels of Nonspherical Nuclei in the Region $150 < A < 190$. *Rev. Mod. Phys.* **1971**, *43*, 424–478.
14. Satula, W.; Wyss, R.; Magierski, P. The Lipkin–Nogami formalism for the cranked mean field. *Nucl. Phys. A* **1994**, *578*, 45–61. [CrossRef]
15. Xu, F.; Satula, W.; Wyss, R. Quadrupole pairing interaction and signature inversion. *Nucl. Phys. A* **2000**, *669*, 119–134. [CrossRef]
16. Zhang, Z.H.; He, X.T.; Zeng, J.Y.; Zhao, E.G.; Zhou, S.G. Systematic investigation of the rotational bands in nuclei with $Z \approx 100$ using a particle–number conserving method based on a cranked shell model. *Phys. Rev. C* **2012**, *85*, 014324. [CrossRef]
17. Hara, K.; Sun, Y. Projected shell model and high–spin spectroscopy. *Int. J. Mod. Phys. E* **1995**, *04*, 637–785. [CrossRef]
18. Shi, Z.; Zhang, H.; Chen, Q.; Zhang, S.; Meng, J. Shell–model–like approach based on cranking covariant density functional theory: Band crossing and shape evolution in ^{60}Fe. *Phys. Rev. C* **2018**, *97*, 034317. [CrossRef]
19. Stelson, P.; Grodzins, L. Nuclear transition probability, $B(E2)$ for $0^+_{g.s.}$–2^+_{first} transitions and deformation parameter, β_2. *Nucl. Data Sheets Sect. A* **1965**, *1*, 21–102. [CrossRef]
20. Raman, S.; Malarkey, C.H.; Milner, W.T.; Nestor, C.W., Jr.; Stelson, P.H. Transition probability, $B(E2)\uparrow$, from the ground to the first–excited 2^+ state of even–even nuclides. *At. Data Nucl. Data Tables* **1987**, *36*, 1–128. [CrossRef]
21. Raman,S.; Nestor, C.W., Jr.; Tikkanen, P. Transition Probability from the Ground to the First–Excited 2^+ State of Even–Even Nuclides. *At. Data Nucl. Data Tables* **2001**, *78*, 1–128. [CrossRef]
22. Reduced Transition Probabilities or $B(E2; 0^+ \rightarrow 2^+)$ Values. Available online: https://www.nndc.bnl.gov/be2 (accessed on 1 December 2022).
23. Pritychenko, B.; Birch, M.; Singh, B.; Horoi, M. Tables of E2 transition probabilities from the first 2^+ states in even–even nuclei. *At. Data Nucl. Data Tables* **2016**, *107*, 1–139. [CrossRef]
24. Pritychenko, B.; Singh, B.; Verpelli, B. Systematic trends of 0^+_2, 1^-_1, 3^-_1 and 2^+_1 excited states in even–even nuclei. *Nucl. Phys. A* **2022**, *1027*, 122511. [CrossRef]
25. Ring, P.; Schuck, P. *The Nuclear Many–Body Problem*; Springer: New York, NY, USA, 1980.
26. Frank, A.; Jolie, J.; van Isacker, P. *Symmetries in Atomic Nuclei: From Isospin to Supersymmetry*, 2nd ed.; Springer: Cham, Switzerland, 2019; ISBN 978-3-030-21930-7.
27. Sheith, J.; Ali, R. Symmetry projection in atomic nuclei. *Eur. Phys. J. Spec. Top.* **2020**, *229*, 2555–2602. [CrossRef]
28. Usmanov, P.; Okhunov, A.; Salikhbaev, U.; Vdonin, A. Analysis of Electromagnetic Transitions in Nuclei ^{176,178}Hf. *Phys. Part. Nucl. Lett.* **2010**, *7*, 185–191. [CrossRef]
29. Okhunov, A.; Turaeva, G.; Kassim, H.; Khandaker, M.; Rosli, N.B. Analysis of the energy spectra of ground states of deformed nuclei in the rare–earth region. *Chin. Phys. C* **2015**, *39*, 044101. [CrossRef]
30. Okhunov, A.; Sharrad, F.; Al-Sammarraie, A.A.; Khandaker, M. Correspondence between phenomenological and IBM-1 models of even isotopes of Yb. *Chin. Phys. C* **2015**, *39*, 084101. [CrossRef]
31. Wiederhold, J.; Werner, V.; Kern, R.; Pietralla, N.; Bucurescu, D.; Carroll, R.; Cooper, N.; Daniel, T.; Filipescu, D.; Florea, N.; et al. Evolution of $E2$ strength in the rare-earth isotopes ^{174,176,178,180}Hf. *Phys. Rev. C* **2019**, *99*, 024316. [CrossRef]
32. Qasim, H.N.; Al-Khudair, F.H. Nuclear shape phase transition in even-even $^{158–168}$Hf isotopes. *Nucl. Phys. A* **2020**, *1002*, 121962. [CrossRef]
33. Das, M.; Biswal, N.; Panda, R.; Bhuyan, M. Structural evolution and shape transition in even-even Hf-isotopes within the relativistic mean-field approach. *Nucl. Phys. A* **2022**, *1019*, 122380. [CrossRef]
34. Vasileiou, P.; Mertzimekis, T.; Chalil, A.; Zyriliou, A.; Pelonis, S.; Efstathiou, M.; Lagaki, V.; Siltzovalis, G.; Koseoglou, P.; Bonatsos, D.; et al. Experimental Investigation of the Nuclear Structure in the Neutron–Rich ^{180}Hf. *Bulg. J. Phys.* **2021**, *48*, 618–624. [CrossRef]
35. Mertzimekis, T.; Vasileiou, P.; Zyriliou, A.; Efstathiou, M.; Chalil, A.; Pelonis, S.; Lagaki, V.; Siltzovalis, G.; Koseoglou, P.; Bonatsos, D.; et al. Experimental Investigations of Nuclear Structure around A = 180. *Bulg. J. Phys.* **2021**, *48*, 625–633. [CrossRef]
36. Zyriliou, A.; Mertzimekis, T.; Chalil, A.; Vasileiou, P.; Pelonis, S.; Efstathiou, M.; Mavrommatis, E.; Bonatsos, D.; Martinou, A.; Peroulis, S.; et al. Reviewing Nuclear Structure Properties of Even–Even Yb Isotopes. *Bulg. J. Phys.* **2021**, *48*, 608–617. [CrossRef]
37. Zyriliou, A.; Mertzimekis, T.J.; Chalil, A.; Vasileiou, P.; Mavrommatis, E.; Bonatsos, D.; Martinou, A.; Peroulis, S.; Minkov, N. A study of some aspects of the nuclear structure in the even–even Yb isotopes. *Eur. Phys. J. Plus* **2022**, *137*, 352. [CrossRef]
38. Krane, K.S. *Introductory Nuclear Physics*; Wiley: New York, NY, USA, 1988.

39. Sharon, Y.; Benczer-Koller, N.; Kumbartzki, G.; Zamick, L.; Casten, R. Systematics of the ratio of electric quadrupole moments $Q(2_1^+)$ to the square root of the reduced transition probabilities $B(E2;0_1^+ \to 2_1^+)$ in even–even nuclei. *Nucl. Phys. A* **2018**, *980*, 131–142. [CrossRef]
40. Bohr, A.; Mottelson, B. Collective and Individual–Particle Aspects of Nuclear Structure. *Mat. Fys. Medd. Dan. Vid. Selsk.* **1953**, *27*, 1–174.
41. Rowe, D.J. *Nuclear Collective Motion*; Metheuen: London, UK, 1970; p. 21.
42. Grodzins, L. The uniform behaviour of electric quadrupole transition probabilities from first 2^+ states in even–even nuclei. *Phys. Lett.* **1962**, *2*, 88–91. [CrossRef]
43. Pritychenko, B.; Birch, M.; Singh, B. Revisiting Grodzins systematics of $B(E2)$ values. *Nucl. Phys. A* **2017**, *962*, 73–102. [CrossRef]
44. Habs, D.; Kester, O.; Ames, F.; Sieber, T.; Bongers, H.; Emhofer, S.; Loewe, M.; Reiter, P.; Lutter, R.; Thirolf, P.; et al. CERN Proposal INTC-P-156. 2002. Available online: https://cds.cern.ch/record/000545918 (accessed on 1 December 2022).
45. Usmanov, P.; Mikhailov, I. Non–adiabatic effects of collective motion in even–even deformed nuclei. *Phys. Part. Nucl. Lett.* **1997**, *28*, 348. [CrossRef]
46. Bertulani, C.A. *Nuclear Physics in a Nutshell*; Princeton University Press: Princeton, NJ, USA, 2007.
47. Harris, S.M. Higher Order Corrections to the Cranking Model. *Phys. Rev.* **1965**, *138*, B509–B513. [CrossRef]
48. Casten, R.F. *Nuclear Structure from a Simple Perspective*; Oxford University Press: Oxford, UK , 2000.
49. He, X.T.; Cao, Y.; Gan, X.L. Effects of high-j orbitals, pairing, and deformed neutron shells on upbendings of ground-state bands in the neutron-rich even-even isotopes $^{170–184}$Hf. *Phys. Rev. C* **2020**, *102*, 014322. [CrossRef]
50. Möller, P.; Nix, J. Nuclear Masses from a Unified Macroscopic–Microscopic Model. *At. Data Nucl. Data Tables* **1988**, *39*, 213–223. [CrossRef]
51. Möller, P.; Nix, J.; Myers, W.; Swiatecki, W. Nuclear ground–state masses and deformations. *At. Data Nucl. Data Tables* **1995**, *59*, 185–381. [CrossRef]
52. Möller, P.; Sierk, A.; Ichikawa, T.; Sagawa, H. Nuclear ground–state masses and deformations: FRDM(2012). *At. Data Nucl. Data Tables* **2016**, *109–110*, 1–204. [CrossRef]
53. Myers, W.; Swiatecki, W. Average nuclear properties. *Ann. Phys.* **1969**, *55*, 395–505. [CrossRef]
54. Strutinsky, V. Shell effects in nuclear masses and deformation energies. *Nucl. Phys. A* **1967**, *95*, 420–442. [CrossRef]
55. Lipkin, H. Collective motion in many–particle systems: Part 1. The violation of conservation laws. *Ann. Phys.* **1960**, *9*, 272–291. [CrossRef]
56. Nogami, Y. Improved Superconductivity Approximation for the Pairing Interaction in Nuclei. *Phys. Rev.* **1964**, *134*, B313–B321. [CrossRef]
57. Möller, P.; Nix, J. Calculation of fission barriers with the droplet model and folded Yukawa single–particle potential. *Nucl. Phys. A* **1974**, *229*, 269–291. [CrossRef]
58. Tondeur, F.; Goriely, S.; Pearson, J.; Onsi, M. Towards a Hartree–Fock Mass Formula. *Phys. Rev. C* **2000**, *62*, 024308. [CrossRef]
59. Goriely, S.; Tondeur, F.; Pearson, J. A Hartree–Fock Nuclear Mass Table. *At. Data Nucl. Data Tables* **2001**, *77*, 311–381. [CrossRef]
60. Goriely, S. Capture Gamma-Ray Spectroscopy and Related Topics. In Proceedings of the 10th International Symposium, Santa Fe, NM, USA, 30 August–3 September 1999; Volume 529, pp. 287–294.
61. Dechargé, J.; Gogny, D. Hartree–Fock–Bogolyubov calculations with the D1 effective interaction on spherical nuclei. *Phys. Rev. C* **1980**, *21*, 1568–1593. [CrossRef]
62. Berger, J.; Girod, M.; Gogny, D. Time–dependent quantum collective dynamics applied to nuclear fission. *Comput. Phys. Commun.* **1991**, *63*, 365–374. [CrossRef]
63. Hilaire, S.; Girod, D. Large-scale mean-field calculations from proton to neutron drip lines using the D1S Gogny force. *Eur. Phys. J. A* **2007**, *33*, 237–241. [CrossRef]
64. Hartree–Fock–Bogoliubov Results Based on the Gogny Force. 2006. Available online: http://www-phynu.cea.fr/science_en_ligne/carte_potentiels_microscopiques/carte_potentiel_nucleaire_eng.htm (accessed on 9 March 2021).
65. Delaroche, J.P.; Girod, M.; Libert, J.; Goutte, H.; Hilaire, S.; Péru, S.; Pillet, N.; Bertsch, G. Structure of even-even nuclei using a mapped collective Hamiltonian and the D1S Gogny interaction. *Phys. Rev. C* **2010**, *81*, 014303. [CrossRef]
66. Kortelainen, M.; McDonnell, J.; Nazarewicz, W.; Reinhard, P.G.; Sarich, J.; Schunck, N.; Stoitsov, M.; Wild, S. Nuclear energy density optimization: Large deformations. *Phys. Rev. C* **2012**, *85*, 024304. [CrossRef]
67. Mass Explorer UNEDF Project. Available online: http://massexplorer.frib.msu.edu/content/DFTMassTables.html (accessed on 20 February 2021).
68. Furnstahl, R. EFT for DFT. In *Lecture Notes in Physics*; Springer: Berlin/Heidelberg, Germany, 2012 ; pp. 133–191. [CrossRef]
69. Agbemava, S.; Afanasjev, A.; Ray, D.; Ring, P. Global performance of covariant energy density functionals: Ground state observables of even–even nuclei and the estimate of theoretical uncertainties. *Phys. Rev. C* **2014**, *89*, 054320. [CrossRef]
70. Agbemava, S.; Afanasjev, A.; Tanina, A. Propagation of statistical uncertainties in covariant density functional theory: Ground state observables and single–particle properties. *Phys. Rev. C* **2019**, *99*, 014318. [CrossRef]
71. Lalazissis, G.; Köning, J.; Ring, P. New parametrization for the Lagrangian density of relativistic mean field theory. *Phys. Rev. C* **1997**, *55*, 540–543. [CrossRef]
72. Gambhir, X.; Ring, P.; Thimet, A. Relativistic Mean Field Theory for Finite Nuclei. *Ann. Phys.* **1990**, *198*, 132–179. [CrossRef]
73. Walecka, J. A theory of highly condensed matter. *Ann. Phys.* **1974**, *83*, 491–529. [CrossRef]

74. Serot, B.D.; Walecka, J.D. The Relativistic Nuclear Many Body Problem. *Adv. Nucl. Phys.* **1986**, *16*, 1–327.
75. Lalazissis, G.; Karatzikos, S.; Fossion, R.; Arteaga, D.P.; Afanasjev, A.; Ring, P. The effective force NL3 revisited. *Phys. Lett. B* **2009**, *671*, 36–41. [CrossRef]
76. Afanasjev, A.V.; Agbemava, S.E.; Ray, D.; Ring, P. Neutron drip line: Single–particle degrees of freedom and pairing properties as sources of theoretical uncertainties. *Phys. Rev. C* **2015**, *91*, 014324. [CrossRef]
77. Boguta, J.; Bodmer, A. Relativistic calculation of nuclear matter and the nuclear surface. *Nucl. Phys. A* **1977**, *292*, 413–428. [CrossRef]
78. Stone, N. Table of nuclear electric quadrupole moments. *At. Data Nucl. Data Tables* **2016**, *111–112*, 1–28. [CrossRef]
79. Warda, M.; Staszczak, A.; Próchniak, L. Comparison of Self–Consistent Skyrme and Gogny Calculations for Light Hg Isotopes. *Int. J. Mod. Phys. E* **2010**, *19*, 787. [CrossRef]
80. Dobaczewski, J.; Afanasjev, A.; Bender, M.; Robledo, L.; Shi, Y. Properties of nuclei in the nobelium region studied within the covariant, Skyrme, and Gogny energy density functionals. *Nucl. Phys. A* **2015**, *944*, 388–414. [CrossRef]
81. Vargas, C.E.; Velázquez, V.; Lerma, S. Microscopic study of neutron–rich dysprosium isotopes. *Eur. Phys. J. A* **2013**, *49*, 4. [CrossRef]
82. Rath, A.K.; Stevenson, P.D.; Regan, P.H.; Xu, F.R.; Walker, P.M. Self-consistent description of dysprosium isotopes in the doubly midshell region. *Nucl. Phys. Group* **2003**, *68*, 10. [CrossRef]
83. Patel, Z.; Söderström, P.A.; Podolyák, Z.; Regan, P.H.; Walker, P.M.; Watanabe, H.; Ideguchi, E.; Simpson, G.S.; Liu, H.L.; Nishimura, S.; et al. Isomer Decay Spectroscopy of ^{164}Sm and ^{166}Gd: Midshell Collectivity Around $N = 100$. *Phys. Rev. Lett.* **2014**, *113*, 262502. [CrossRef]
84. Ideguchi, E.; Simpson, G.S.; Yokoyama, R.; Tanaka, M.; Nishimura, S.; Doornenbal, P.; Lorusso, G.; Söderström, P.A.; Sumikama, T.; Wu, J.; et al. µs isomers of ^{158,160}Nd. *Phys. Rev. C* **2016**, *94*, 064322. [CrossRef]